A Learning Approach for Suture Thread Detection With Feature Enhancement and Segmentation for 3-D Shape Reconstruction

Bo Lu, X. B. Yu, J. W. Lai, K. C. Huang, Keith C. C. Chan, and Henry K. Chu, *Member, IEEE*

***Abstract*— A vision-based system presents one of the most reliable methods for achieving an automated robot-assisted manipulation associated with surgical knot tying. However, some challenges in suture thread detection and automated suture thread grasping significantly hinder the realization of a fully automated surgical knot tying. In this article, we propose a novel algorithm that can be used for computing the 3-D coordinates of a suture thread in knot tying. After proper training with our data set, we built a deep-learning model for accurately locating the suture's tip. By applying a Hessian-based filter with multiscale parameters, the environmental noises can be eliminated while preserving the suture thread information. A multistencils fast marching method was then employed to segment the suture thread, and a precise stereomatching algorithm was implemented to compute the 3-D coordinates of this thread. Experiments associated with the precision of the deep-learning model, the robustness of the 2-D segmentation approach, and the overall accuracy of 3-D coordinate computation of the suture thread were conducted in various scenarios, and the results quantitatively validate the feasibility and reliability of the entire scheme for automated 3-D shape reconstruction.**

***Note to Practitioners*—This article was motivated by the challenges of suture thread detection and 3-D coordinate evaluation in a calibrated stereovision system. To precisely detect the suture thread with no distinctive feature in an image, additional information, such as the two ends of the suture thread or its total length, is usually required. This article suggests a new method utilizing a deep-learning model to automate the tip detection process, eliminating the need of manual click in the initial stage. After feature enhancements with image filters, a multistencils fast marching method was incorporated to compute the arrival time from the detected tip to other points on the suture contour. By finding the point that takes the maximal time to travel in a closed contour, the other end of the suture thread can be identified, thereby allowing suture threads of any length to be segmented out from an image. A precise stereomatching method was then proposed to generate matched key points of the suture thread on the image pair, thereby enabling the reconstruction of its 3-D coordinates. The accuracy and robustness of the entire suture detection scheme were validated through experiments with different backgrounds and lengths. This proposed scheme offers a new solution for detecting curvilinear objects and their 3-D coordinates, which shows potential in realizing automated suture grasping with robot manipulators.**

***Index Terms*— 3-D coordinates computation, stereovision, surgical robot, suture thread detection.**

I. Introduction

ROBOT-ASSISTED manipulation (RAM) is a widely employed technology in minimally invasive surgery (MIS) [1] that allows surgeons to perform precise operations with high dexterity [2], manipulability [3], and complexity [4]. These manipulating systems are manually controlled by surgeons through a master–slave device, and real-time 2-D images are available for monitoring [5]. However, despite assistance from robotic systems, surgeons may feel tired after a long period of operation because staring at the screen for an extended period can cause eyesore and irritation, which, in turn, may lead to misoperations and secondary trauma to tissues [6]. To improve the performance of RAM, automated manipulation can be incorporated into some low-level operations in surgery [7] by standardizing the procedure of path planning [8] or by improving robustness via visual [9] and force feedback [10]. Reducing the amount of human intervention can improve the overall operating efficiency of RAM.

Surgical knot tying is a popular manipulation that can be performed by robots in an automated or semiautomated manner. The operation begins with suture threading, in which a suture is stitched through the wound automatically by using robotic arms. Sen *et al.* [11] proposed a multithrow stitching method based on a sequential convex programming by using a 3-D printed suture needle angle positioner. Pedram *et al.* [12] developed a kinematic model that describes the needle–tissue interaction and can be used for constant curvature needle path planning by using information about the tissue geometry, the surgeon-defined entry/exit points, and the optimization weighting factors.

To tighten a surgical knot, suture loops must be formed with the suture thread. To form a high-quality loop, trajectory planning and the optimization of the control scheme have

Manuscript received July 15, 2019; accepted October 16, 2019. Date of publication November 26, 2019; date of current version April 7, 2020. This article was recommended for publication by Associate Editor X. Li and Editor Y. Sun upon evaluation of the reviewers' comments. This work was supported in part by the Research Grant Council of the Hong Kong Special Administrative Region, China, under Grant 25204016. *(Corresponding author: Henry K. Chu.)*

B. Lu was with the Department of Mechanical Engineering, The Hong Kong Polytechnic University, Hong Kong. He is now with the T-stone Robotics Institute, The Chinese University of Hong Kong, Hong Kong (e-mail: bo.lu@connect.polyu.hk).

J. W. Lai, K. C. Huang, and H. K. Chu are with the Department of Mechanical Engineering, The Hong Kong Polytechnic University, Hong Kong (e-mail: henry.chu@polyu.edu.hk).

X. B. Yu and K. C. C. Chan are with the Department of Computing, The Hong Kong Polytechnic University, Hong Kong.

This article has supplementary downloadable material available at http://ieeexplore.ieee.org, provided by the authors.

Color versions of one or more of the figures in this article are available online at http://ieeexplore.ieee.org.

Digital Object Identifier 10.1109/TASE.2019.2950005

been studied. Osa *et al.* [13] proposed a framework that can learn the spatial motion and force information from previous trials for online trajectory planning and automated suture looping in a dynamic environment. Lu *et al.* [9] generated a space-efficient trajectory for robot-assisted suture looping manipulation and found that the entire operation can achieve sufficient accuracy and robustness by using a visual guide, an online optimizer, and a dynamic linear quadratic (LQ) controller.

However, the works mentioned in [11] and [12] have mainly focused on the stitching part of the process. Afterward, the long suture thread needs to be trimmed in order to form loops before tying a surgical knot. Due to its flexible property, the suture thread may form various shapes arbitrarily on the tissue or the skin surface. To automate the knot-tying task, the 3-D coordinates of the suture thread must be accurately determined to facilitate its grasping operation, the suture thread stitching, and the subsequent looping manipulation using robots.

An RGB-D camera is often used to obtain the 3-D information of the suture thread. Mohanarajah *et al.* [14] used the point cloud by running a dense odometry algorithm in collaborative robots and achieved a 3-D visualization of the surroundings. Stereocamera is another popular paradigm for 3-D scene reconstruction. Ren *et al.* [15] proposed a dual-camera-based method that uses markers for surgical tracking. However, these approaches either rely on feature descriptors or markers, which can hardly cope with the detection of a long, flexible, and featureless surgical suture thread.

To address this challenge, the segmentation and stereopair matching of a curvilinear object in a stereocamera system are necessary. Jackson *et al.* [16] proposed a stereoimage-based algorithm that detects the suture thread by using a B-spline model. By minimizing the image matching energy, they can track the suture thread in real time. Obara *et al.* [17] proposed a contrast-independent method that uses the phase congruency tensor to segment the curvilinear object from noisy biomedical images. Benmansour and Cohen [18] adopted the fast marching method (FMM) to identify the closed contour or surface with two endpoints in both 2-D and 3-D images. Kaul *et al.* [19] also adopted the FMM principle to detect both open and closed curves with a single starting input.

In recent years, deep-learning approaches have been extensively used for accurate object detection. For instance, Cha and Choi [20] proposed a vision-based inspection method for detecting cracks on concrete images by using a convolutional neural network (CNN). They later improved this algorithm to the faster region-based CNN (Faster R-CNN) for detecting multiple types of damages [21]. Chen and Jahanshahi [22] combined CNN and naive Bayes data fusion for inspecting the cracks of a nuclear power plant. Their work mainly focused on detecting crack features on a 2-D image where object segmentation is not required for its length evaluation. In this article, a recurrent neural network (RNN) was employed for tip detection in a temporal sequence of 2-D images (or to model the temporal dependence) [23], and several new algorithms were implemented for suture length evaluation and 3-D shape computation.

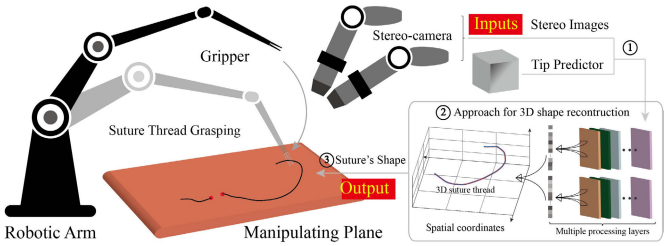

Fig. 1. System illustration for suture thread 3-D reconstruction.

In this article, we present a novel approach for constructing the 3-D model of a surgical suture thread in an arbitrary environment. First, to reduce the need for manually clicking on two ends of a suture, we employ a neural network to automatically locate the suture's tip on the image. Given that tips with less distinctive features can easily result in ambiguous matches in the nearby region, a long short-term memory (LSTM) was incorporated to avoid a repeated detection of the same object. To address the challenges in finding flexible and thin sutures for segmentation, a Hessian-matrix-based filter was employed for feature enhancement and noise suppression. Due to the ambiguity of the Hessian eigenvectors' directions in detecting curvilinear objects [17], [24], a numerical multistencils FMM (MFMM) [25] was applied to compute the arrival time map, which determines the minimal arrival time from each pixel in the image to the suture thread's tip. Using this information, the object can be completely segmented along the object contour in a 2-D plane. While the method proposed in [18] and [26] requires additional information such as the endpoint or the object length, this article evaluates the endpoint (turning) by finding the point that takes the longest time to reach from the tip in a closed contour. By combining the map with the proposed front and back propagations, precise key points can be assigned, matched, and visually corrected [27] along the suture thread for the 3-D computation on the left and right images. As shown in Fig. 1, by using stereoimages as inputs, the 3-D coordinates of the suture thread from one end to the other can be evaluated and outputted accordingly.

The rest of this article is organized as follows. Section II introduces the deep-learning model for the suture's tip detection. In Section III, the procedures for highlighting and segmenting the curvilinear object will be proposed. Section IV presents the principle of the MFMM and its implementation for suture detection. Besides, the segmentation of the suture thread, its key point generation, and the stereomatching will be introduced. Section V provides the experimental results of the tip point detection using the deep-learning model, the robustness of 2-D suture thread segmentation, and the accuracy of computing its 3-D coordinates under various environments. Section VI concludes this article.

II. Initialization Using the Deep-Learning Approach

A. Deep-Learning Model for Suture Thread's Tip Detection

To locate the suture's tip in an image, we used the deep-learning-based object detection model proposed by Stewart *et al.* [23], which uses a CNN ImageNet for feature

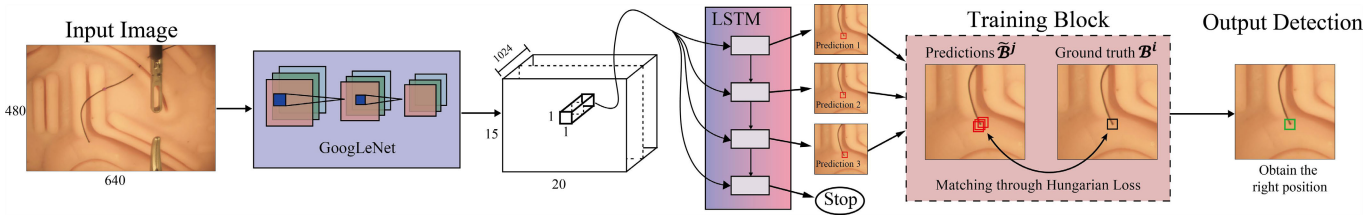

Fig. 2. General framework of the deep-learning model. Using our own data set to train the model, the LSTM can act as a controller for the suture thread's tip detection. With the implementation of the Hungarian Loss, the optimal position of the suture thread's tip can be picked out from the image.

encoding and an RNN with LSTM units to sequentially decode bounding boxes, as shown in Fig. 2.

The advantage of ImageNet lies in its representational power to encode multiple objects, thereby providing enough robustness for extracting a single suture's tip. LSTM can memorize the previous output of the bounding box and then feed this output as input to the next layer for modeling the generation sequence of the next bounding box. Given that the generated sequence will not be duplicately produced in the later stage when conducting object detection, the whole procedure can proceed effectively.

To reduce the computation cost, the image is compressed into 640×480 pixels, and then, a new bounding box and the confidence that this box includes the undetected suture thread's tip will be computed as the output in each layer of LSTM. Boxes are produced in a descending confidence order, and each new detection will be conditioned based on the previous one. By using a prespecified threshold, the detection is terminated when the LSTM is unable to find a new box with a confidence above the threshold value. Until this stage, the output sequence can be collected and presented as a final description of all object instances in the region. In our task, the desired target is a single suture thread's tip. Given that LSTM will output a prediction set of bounding boxes, as shown in Fig. 2, we employed an optimizer to find the optimal position of the suture's tip from the detected candidates.

B. Optimization Using Loss Function

By assuming the outputs of the collected sequential candidates as $\mathcal{O}$ which is shown in Fig. 2, we utilized the Hungarian algorithm [23] to model the bipartite matching between the predicted outputs $\mathcal{O}$ and the ground truth $\mathcal{G}$ in polynomial time. The loss function associated with the Hungarian algorithm which models the distance between the predicted outputs $\mathcal{O} = \left\{\tilde{\mathcal{B}}^j | j = 1, 2, \ldots, N\right\}$ and the ground truths $\mathcal{G} = \left\{\mathcal{B}^i | i = 1, 2, \ldots, N\right\}$ follows:

$$L(\mathcal{G}, \mathcal{O}, f) = \nu \sum_{i=1}^{|\mathcal{G}|} l_{\text{pos}}\left(\mathcal{B}^i_{\text{pos}}, \tilde{\mathcal{B}}^{f(i)}_{\text{pos}}\right) + \sum_{j=1}^{|\mathcal{O}|} l_c(\tilde{\mathcal{B}}^j_c, y_j) + \sum_{i=1}^{|\mathcal{G}|}\sum_{j=1}^{|\mathcal{O}|} \Delta\left(\mathcal{B}^i, \tilde{\mathcal{B}}^j\right) \quad (1)$$

where the localization accuracy is equal to $l_{\text{pos}} = ||\mathcal{B}^i_{\text{pos}} - \tilde{\mathcal{B}^{f(i)}_{\text{pos}}}||_1$ and represents the displacement between the positions of the ground truth and the candidates. The detection confidence l_c determines the cross-entropy loss on a candidate's confidence to the match of the ground truth, and f denotes the bipartite matching between $\mathcal{O}$ and $\mathcal{G}$ in polynomial time as obtained by the Hungarian algorithm.

III. Image Filter for Curvilinear Object Segmentation

With the detected tip, the following step is to segment the suture thread from the background. In various conditions, an image may contain undesired noises that need to be filtered using proper image filters before the object segmentation.

Several image denoising and enhancement filters have been comprehensively developed, including the smooth filter [28], Gaussian filter [29], max–min filter [30], and weighted median filter [31]. However, these filters do not show satisfactory performance in segmenting curvilinear objects. In order to enhance the curvilinear information, the second derivatives with the Gaussian kernel are implemented [32].

For a stereocamera, the 2-D left and right frames can be denoted as $\mathbb{C}_l$ and $\mathbb{C}_r$, and their respective image domains can be denoted as $\Omega_l, \Omega_r \rightarrow \mathbb{R}^+$, where the subscripts l and r denote the left and right cameras, respectively. To distinguish curvilinear features at various conditions, a multiple scale parameter σ_i was implemented.

By taking one camera frame for example, after transforming the color image into grayscale, the local behavior of point $\mathbf{p}_i \in \Omega$ can be determined as its Taylor expansion as

$$\mathbb{C}(\mathbf{p}_i + \Delta\mathbf{p}_i, \sigma_i) \approx \mathbb{C}(\mathbf{p}_i, \sigma_i) + \delta\mathbf{p}_i^T \nabla_{i,\sigma_i} + \delta\mathbf{p}_i^T \mathcal{H}_{i,\sigma_i} \delta\mathbf{p}_i \quad (2)$$

where the expansion approximates the image structure up to the second-order derivatives, while ∇_{i,σ_i} and $\mathcal{H}_{i,\sigma_i}$ denote the gradient vector and the corresponding Hessian matrix that are computed at scale σ_i [33]. To highlight the curvilinear information, we processed the image by applying a Gaussian filter with a size of $(3\sigma_i + 1) \times (3\sigma_i + 1)$. The 2-D Gaussian filter is defined as

$$G(\mathbf{p}_{\text{gau}}, \sigma_i) = \frac{1}{2\pi\sigma_i^2} \cdot \mathrm{e}^{-\frac{||\mathbf{p}_{\text{gau}}||^2}{2\sigma_i^2}} \quad (3)$$

where $\mathbf{p}_{\text{gau}} = [\mathbf{X}_G, \mathbf{Y}_G]$ is the image coordinates of the filter. Based on (2), the third term of the Taylor series gives the second derivatives of image $\mathbb{C}$, with $\mathcal{H}$ being the Hessian matrix, which can be expressed as

$$\mathcal{H}(\sigma_i) = \begin{bmatrix} \boldsymbol{I}_{xx}(\sigma_i) & \boldsymbol{I}_{xy}(\sigma_i) \\ \boldsymbol{I}_{xy}(\sigma_i) & \boldsymbol{I}_{yy}(\sigma_i) \end{bmatrix}. \quad (4)$$

According to the scale-space theory, the Hessian matrix can be represented by the convolution between the second derivatives of the Gaussian filter and the image as follows:

$$\begin{cases} \boldsymbol{I}_{xx}(\sigma_i) = \frac{\partial^2}{\partial x^2}\mathbb{C}(\sigma_i) = \sigma_i^{\gamma} \cdot \frac{\partial^2}{\partial x^2} G(\mathbf{p}_{\text{gau}}, \sigma_i) \otimes \mathbb{C}(\sigma_i) \\ \boldsymbol{I}_{xy}(\sigma_i) = \frac{\partial^2}{\partial x \partial y}\mathbb{C}(\sigma_i) = \sigma_i^{\gamma} \cdot \frac{\partial^2}{\partial x \partial y} G(\mathbf{p}_{\text{gau}}, \sigma_i) \otimes \mathbb{C}(\sigma_i) \\ \boldsymbol{I}_{yy}(\sigma_i) = \frac{\partial^2}{\partial y^2}\mathbb{C}(\sigma_i) = \sigma_i^{\gamma} \cdot \frac{\partial^2}{\partial y^2} G(\mathbf{p}_{\text{gau}}, \sigma_i) \otimes \mathbb{C}(\sigma_i) \end{cases} \tag{5}$$

where $\otimes$ is the image convolutional operator. We also added a parameter γ to normalize the derivatives following the suggestions of Lindeberg [34]. This parameter is restricted as $0 < \gamma < 3$ [35]. To denote the second derivatives of the Gaussian filter, $\boldsymbol{h}$ can be computed with respect to scale σ_i as

$$\boldsymbol{h}(\sigma_i) = \begin{bmatrix} \mathbf{h}_{xx}(\sigma_i) \\ \mathbf{h}_{xy}(\sigma_i) \\ \mathbf{h}_{yy}(\sigma_i) \end{bmatrix} = \begin{bmatrix} \frac{1}{2\pi \cdot \sigma_i^4} \cdot \left(\frac{\mathbf{X}_G^2}{\sigma_i^2} - 1 \right) \cdot \mathrm{e}^{\frac{-\left(\mathbf{X}_G^2 + \mathbf{Y}_G^2\right)}{2\sigma_i^2}} \\ \frac{1}{2\pi \cdot \sigma_i^6} \cdot \boldsymbol{X}_G \cdot \boldsymbol{Y}_G \cdot \mathrm{e}^{\frac{-\left(\mathbf{X}_G^2 + \mathbf{Y}_G^2\right)}{2\sigma_i^2}} \\ \mathbf{h}_{xx}^T(\sigma_i) \end{bmatrix}. \tag{6}$$

For dark lines on a bright background, the Gaussian kernel returns large positive values across the line and small (positive or negative) values along the line, which can be explained by the eigenvalues of the Hessian matrix [35].

The line structures can be detected by analyzing the Hessian matrix and its eigenvalues. Let the eigenvalues of $\mathcal{H}(\sigma_i)$ be $\lambda_1(\sigma_i)$ and $\lambda_2(\sigma_i)$, and the filtered image $\mathbb{T}(\sigma_i)$ of $\mathbb{C}(\sigma_i)$ can be computed as

$$\mathbb{T}(\sigma_i) = \begin{cases} 0, & \lambda_2(\sigma_i) < 0 \\ \mathrm{e}^{-\frac{\mathcal{R}_{b,\sigma_i}^2}{2\beta^2}} \cdot \left(\boldsymbol{I} - \mathrm{e}^{-\frac{\mathcal{S}_{\sigma_i}^2}{2\mathcal{C}^2}} \right), & \text{otherwise} \end{cases} \tag{7}$$

where $\mathcal{R}_{b,\sigma_i} = \lambda_1(\sigma_i)/\lambda_2(\sigma_i)$, $\mathcal{S}_{\sigma_i} = (\lambda_1(\sigma_i) + \lambda_2(\sigma_i))^{1/2}$, β, and $\mathcal{C}$ are the threshold parameters that control the sensitivity of the filter to the measures of $\mathcal{R}_b$ and $\mathcal{S}$, respectively [36]. By repeating the above procedures with different scale parameters σ_i, the optimal image can be chosen [34] at the local maxima as follows:

$$\mathbb{T} = \max_{\sigma_{\min} \le \sigma_i \le \sigma_{\max}} \mathbb{T}(\sigma_i). \tag{8}$$

By setting a proper threshold, $\mathbb{T}$ can be converted into a binary image in which the surrounding noises are initially eliminated.

IV. Suture Thread Segmentation and Key Point Matching

To compute the 3-D coordinates of a suture thread, sufficient numbers of key points and their respective stereopairs should be obtained. Therefore, an accurate description of the suture thread from its tip to the end is required.

To achieve this goal, the minimal action map [18] was computed by using the images $\mathbb{T}$ captured from the camera frame. Within a 2-D image, its form of energy E can be expressed as

$$E(\phi) = \int_{\phi} \{\mathcal{P}(\phi(\varepsilon)) + w\} d\epsilon = \int_{\phi} \widetilde{\mathcal{P}}(\phi(\varepsilon) d\epsilon \tag{9}$$

where ϕ denotes the curve within the image domain $\Omega \to R^+$, and $\mathcal{P}$ is the potential image of the input image $\mathbb{T}$. The minimal action map highlights the curvilinear information, and the choice of $\mathcal{P}$ depends on the specific application. In our task, we set $\mathcal{P}$ as

$$\mathcal{P} = (s \cdot \nabla \mathbb{T} + \xi)^{-4} \tag{10}$$

where s is a parameter that highlights the variation along the suture thread boundary, and ξ and ω in (9) and (10) are small positive constants that can be tuned by users. The value of $(1/\widetilde{\mathcal{P}})$ represents the traveling speed when crossing each pixel. Therefore, our potential function aims to set the boundary of the suture thread with a high traveling speed, while the background pixels with slow traveling velocities.

By treating the detected tip $\mathbf{p}_t$ as the source point, for any point $\mathbf{p}_i \in \Omega$, the minimal path denotes the trajectory along which the propagation time between $\mathbf{p}_t$ and $\mathbf{p}_i$ obtains the minimal value. Consequently, the curve ε_i between tip $\mathbf{p}_t$ and point $\mathbf{p}_i$ within the domain Ω that can minimize the energy function E can be determined as

$$\forall \mathbf{p}_i \in \Omega, \mathcal{M}_{(\mathbf{p}_i)} = \min_{\phi \in \text{Path}_{\mathbf{p}_t, \mathbf{p}_i}} \left\{ \int_{\phi} \widetilde{\mathcal{P}}(\phi(\varepsilon) d\epsilon \right\} \tag{11}$$

where $\text{Path}_{\mathbf{p}_t, \mathbf{p}_i}$ denotes all paths that connect point $\mathbf{p}_i$ to source point $\mathbf{p}_t$ within Ω. Traveling along a minimal time path, $\mathcal{M}(\mathbf{p}_i)$ denotes the arrival time between $\mathbf{p}_i$ and $\mathbf{p}_t$. When traveling across point $\mathbf{p}_j$, the velocity only depends on the value $(1/\widetilde{\mathcal{P}}_{(\mathbf{p}_j)})$ [37] and satisfies the Eikonal equation as

$$\begin{cases} ||\nabla \mathcal{M}_{(\mathbf{p}_i)}|| = \widetilde{\mathcal{P}}_{(\mathbf{p}_i)}, & \mathbf{p}_i \in \Omega \\ \mathcal{M}_{(\mathbf{p}_t)} = 0. \end{cases} \tag{12}$$

For each point $\mathbf{p}_i$ within the image, the original pixel value can be substituted by its arrival time $\mathcal{M}_{(\mathbf{p}_i)}$. Therefore, the arrival time map of the corresponding input image can be obtained. To achieve this goal, the fast marching method (FMM) developed in [25] was incorporated into our scheme.

A. General Principle and Derivation of FMM

To obtain the arrival time from any point to the source point, the method proposed by Rouy and Tourin [38] along with the solution of the correct viscosity was implemented. For point $[i, j] \in \Omega$, the equation approximated using the first-order finite difference in a discrete format can be obtained as

$$\max\left\{ \frac{\mathcal{M}_{(i,j)} - \mathcal{M}_x}{\triangle_x}, 0 \right\}^2 + \max\left\{ \frac{\mathcal{M}_{(i,j)} - \mathcal{M}_y}{\triangle_y}, 0 \right\}^2 = \widetilde{\mathcal{P}}^2(i, j) \tag{13}$$

where $\triangle_x$ and $\triangle_y$ denote the pixel spacing along the horizontal and vertical directions within the image. We also have

$$\begin{aligned} \mathcal{M}_x &= \min\left\{ \mathcal{M}_{(i-1,j)}, \mathcal{M}_{(i+1,j)} \right\} \\ \mathcal{M}_y &= \min\left\{ \mathcal{M}_{(i,j-1)}, \mathcal{M}_{(i,j+1)} \right\}. \end{aligned} \tag{14}$$

The solution of (13) can be solved as follows.

1) $\mathcal{M}_{(i,j)} > \max(\mathcal{M}_x, \mathcal{M}_y)$, where $\mathcal{M}_{(i,j)}$ is the maximum solution of the quadratic equation:

$$\mathcal{M}_{(i,j)} = (((\mathcal{M}_x + \mathcal{M}_y) + \sqrt{2\widetilde{\mathcal{P}}^2(i,j) - (\mathcal{M}_x - \mathcal{M}_y)^2})/(2)).$$

2) $\mathcal{M}_x > \mathcal{M}_{(i,j)} > \mathcal{M}_y$, $\mathcal{M}_{(i,j)} = \mathcal{M}_y + \widetilde{\mathcal{P}}(i,j)$.
3) $\mathcal{M}_y > \mathcal{M}_{(i,j)} > \mathcal{M}_x$, $\mathcal{M}_{(i,j)} = \mathcal{M}_x + \widetilde{\mathcal{P}}(i,j)$.

To finalize the FMM process, all pixels in the entire image domain were labeled with the following sets.

1) *Alive Set* p_{Alive}: For points $\mathbf{p}_i$ belonging to this set, the arrival times $\mathcal{M}_{\mathbf{p}_i}$ have been computed and fixed.
2) *Trial Set* p_{Trial}: Four neighbors around the alive set, and their arrival times may be changed in the later iteration.
3) *Far Set* p_{Far}: For those points that have not been reached, and their arrival times have not been calculated.

Algorithm 1 FMM for the 2-D Image

Data: Image $\mathbb{T}_l$ and $\mathbb{T}_r$, source points $\mathbf{p}_{t,l}$ and $\mathbf{p}_{t,r}$
For each image, the tip of the suture thread is labeled as the alive set, which is initialized as $\mathcal{M}_{\mathbf{p}_t} = 0$;
Four neighbors of $\mathbf{p}_t$ are labeled as the trial set, and their corresponding arrival times $\mathcal{M}_{\mathbf{p}_{Trial}}$ can be computed using Eq. (13);
Set other points as the far set $\mathbf{p}_{far}$: $\mathcal{M}_{\mathbf{p}_{far}} = \infty$;
Pick the local minima of $\mathcal{M}_{\mathbf{p}_{Trial}}$, and sort the corresponding point to the alive set;
Loop the procedure: **while** $\boldsymbol{p}_{far} \neq \varnothing$ **do**
    Exam the four neighbors of the all alive points;
    if *Neighbors* $\notin \boldsymbol{p}_{Alive}$ **then**
        Update the arrival time $\mathcal{M}_{\mathbf{p}_{Trial}}$ using Eq. (13);
        Move point which has the local minima among $\mathcal{M}_{\mathbf{p}_{Trial}}$ to the alive set $\mathbf{p}_{Alive}$;
Result: The map of arrival time $\mathcal{M}_{\mathbf{p}_l}$ and $\mathcal{M}_{\mathbf{p}_r}$ with respect to the source point

The general process of FMM is summarized in Algorithm 1. First, the source point is sorted as the alive set. Afterward, the four neighbors of the alive set are treated as the trial set, and their arrival times can be computed. The point with the minimal action $\mathcal{M}$ among the trial set $\mathcal{M}_{\mathbf{p}_{Trial}}$ can be updated to the alive set. Then, loop the above procedure, and one new point can be updated into the alive set in each iteration. This procedure is terminated when the arrival times of all points within the image domain are determined.

However, FMM only makes use of four neighbors but neglects the diagonal information. In this case, the arrival time amp may not be accurate enough. Moreover, the solution of (13) only uses the first-order approximation, which introduces additional errors when calculating the arrival time map. These shortcomings potentially harm the accuracy of the upcoming suture thread segmentation.

B. Arrival Time Map Computation Using MFMM

To achieve a higher precision and resolve the aforementioned problems, an enhanced method called MFMM [25] was adopted to compute the arrival time map $\mathcal{M}$ while considering the diagonal information.

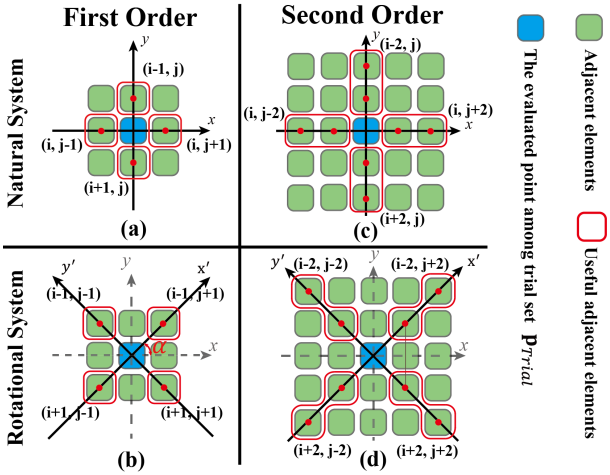

Fig. 3. Normal coordinate using (a) first-order and (c) second-order approximations. The rotated coordinate using (b) first-order and (d) second-order approximations.

Consider that the natural Cartesian coordinate is rotated with an angle α, as shown in Fig. 3(b) and (d). For any point (x, y) in the natural coordinate, its new position (x', y') in the rotated coordinate can be denoted as

$$\begin{aligned} x' &= x\cos\alpha + y\sin\alpha \\ y' &= -x\sin\alpha + y\cos\alpha. \end{aligned} \tag{15}$$

Using the chain rule, the partial derivatives of the arrival time $\mathcal{M}$ with respect to x and y can be derived as

$$\begin{aligned} \mathcal{M}_x &= \frac{\partial \mathcal{M}}{\partial x} = \frac{\partial \mathcal{M}}{\partial x'} \cdot \frac{\partial x'}{\partial x} + \frac{\partial \mathcal{M}}{\partial y'} \cdot \frac{\partial y'}{\partial x} \\ \mathcal{M}_y &= \frac{\partial \mathcal{M}}{\partial y} = \frac{\partial \mathcal{M}}{\partial x'} \cdot \frac{\partial x'}{\partial y} + \frac{\partial \mathcal{M}}{\partial y'} \cdot \frac{\partial y'}{\partial y}. \end{aligned} \tag{16}$$

By substituting (15) into (16) and letting the rotational angle be 45°, we can easily obtain

$$\begin{aligned} &\mathcal{M}_x^2 + \mathcal{M}_y^2 = \frac{\partial^2 \mathcal{M}}{\partial x'^2} + \frac{\partial^2 \mathcal{M}}{\partial y'^2} = \mathcal{M}_{x'}^2 + \mathcal{M}_{y'}^2 \\ &\Rightarrow \widetilde{\mathcal{P}}^2_{(x,y)} = |\nabla \mathcal{M}_{(x',y')}|^2. \end{aligned} \tag{17}$$

It is noticed that (17) is also the Eikonal equation, which indicates that $\nabla \mathcal{M}_{(x',y')}$ in the rotational coordinate can be computed by solving the Eikonal equation along the new directions x' and y'. Therefore, the arrival time along the diagonal direction can also be solved by following the FMM principle in a rotational system. For point $[i, j] \in \Omega$, we have

$$\sum_{\zeta=1}^{2} \max\left\{\mathcal{C}_\zeta \cdot \frac{\mathcal{M}_{(i,j)} - \mathcal{M}_\zeta}{\triangle_\zeta}, 0\right\}^2 = \widetilde{\mathcal{P}}^2(i,j) \tag{18}$$

where $\mathcal{C}_\zeta$ denotes the approximation coefficient, and $\triangle_\zeta$ is the adjacent pixel distance. For a natural system, $\triangle_\zeta$ is equal to 1, whereas for a rotational system, it is equal to $\sqrt{2}$. To further improve the accuracy of the arrival time map, the following

TABLE I
VALUES OF THREE Υ

Coefficient		1st-order	2nd-order
$\Upsilon_{(1)}$	Natural	2	$9/8$
	Rotated	1	$9/16$
$\Upsilon_{(2)}$	Natural	$-2(\mathcal{M}_x+\mathcal{M}_y)$	$-\frac{9}{8}(\mathcal{M}_x+\mathcal{M}_y)$
	Rotated	$-\mathcal{M}_{x'}-\mathcal{M}_{y'}$	$-\frac{9}{16}(\mathcal{M}_{x'}+\mathcal{M}_{y'})$
$\Upsilon_{(3)}$	Natural	$\mathcal{M}_x^2+\mathcal{M}_y^2$	$\frac{9}{4}(\mathcal{M}_x^2+\mathcal{M}_y^2)$
	Rotated	$\frac{1}{2}(\mathcal{M}_{x'}^2+\mathcal{M}_{y'}^2)$	$\frac{9}{8}(\mathcal{M}_{x'}^2+\mathcal{M}_{y'}^2)$

second-order approximation proposed in [39] was adopted:

$$\begin{cases}\mathcal{M}_x = \min\limits_{a_x\in\{1,-1\}}\left[\frac{4\mathcal{M}_{(i+a_x,j)}-\mathcal{M}_{(i+2\cdot a_x,j)}}{3}\right] \\ \mathcal{M}_y = \min\limits_{a_y\in\{1,-1\}}\left[\frac{4\mathcal{M}_{(i,j+a_y)}-\mathcal{M}_{(i,j+2\cdot a_y)}}{3}\right].\end{cases} \tag{19}$$

The selection of the parameters is summarized as follows.

1) Adopting the first-order approximation, $\mathcal{C}_\zeta = 1$, $\mathcal{M}_\zeta$ can be solved by using two adjacent neighbors, as shown in Fig. 3(a) and (b) and by using (14).
2) Adopting the second-order approximation, $\mathcal{C}_\zeta = 3/2$, $\mathcal{M}_\zeta$ can be solved by using (19), whereas the two-pixel away points are provided as shown in Fig. 3(c) and (d).

Equation (18) can then be transformed as

$$\Upsilon_{(1)}\mathcal{M}_{(i,j)}^2 + \Upsilon_{(2)}\mathcal{M}_{(i,j)} + \Upsilon_{(3)} = \widetilde{\mathcal{P}}^2(i,j) \tag{20}$$

where coefficients $\Upsilon_{(1)}$, $\Upsilon_{(2)}$, and $\Upsilon_{(3)}$ are listed in Table I.

Therefore, the arrival time of $\mathcal{M}_{(i,j)}$ can be computed as the minimal positive solution of (20) as follows:

$$\mathcal{M}_{(i,j)} = \frac{-\Upsilon_{(2)} \pm \sqrt{\Upsilon_{(2)}^2 - 4\Upsilon_{(1)}(\widetilde{\mathcal{P}}^2(i,j) - \Upsilon_{(3)})}}{2\Upsilon_{(1)}}. \tag{21}$$

The expansion procedures of the FMM and MFMM when calculating the arrival time map are shown in the Supplementary Material. Starting from the source point, the FMM only expands in the horizontal and vertical directions, whereas the MFMM preserves this property while adding the diagonal expansion. As a result, the narrowband formed by $\mathbf{p}_{\text{Trial}}$ is larger in MFMM than that in FMM. When using the arrival time map to segment the suture thread, the FMM only gives the propagation path in either the horizontal or vertical direction, whereas the MFMM allows the diagonal shape, thereby increasing the precision of reconstructing the 3-D shape of the suture thread.

C. Segmentation and Point Matching of the Suture Thread

With the rectified stereocamera [40], the arrival time map $\mathcal{M}$ and suture thread's tip position $\mathbf{p}_t$ can be obtained. A convenient and accurate stereomatching algorithm was then built for the suture thread's segmentation and matching. Starting from tip point $\mathbf{p}_t$, the potential function gives a larger traveling velocity $(1/\widetilde{\mathcal{P}})$ along the suture contour, and the desired neighbor that connects the tip should be the point that possesses the minimal value $\mathcal{M}_{\min}$.

As shown in Fig. 4, the yellow denotes part of the contour area that has a high traveling speed. Starting from the suture

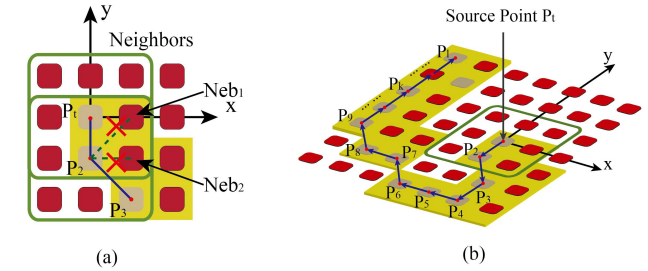

Fig. 4. Selection of the suture thread contour point (a) from the tip position to (b) the whole structure, using the minimal increasing principle.

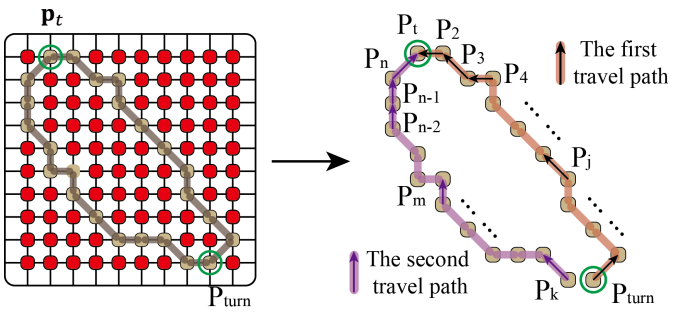

Fig. 5. Illustration of the end (turning point) evaluation.

thread's tip $\mathbf{p}_t$, its eight neighbors are initially evaluated, as shown in Fig. 4(a). The second pixel $\mathbf{p}_2$ was selected based on the minimal increasing principle. It is noticed that Neb_1 and Neb_2 are two neighbors centered at $\mathbf{p}_t$ and $\mathbf{p}_2$. When evaluating the eight neighbors of $\mathbf{p}_2$, Neb_1 or Neb_2 can be selected as connecting elements, which can lead to a trapped zigzag or even a false segmentation result.

To eliminate the potential mistake and the unfavorable zigzag shapes, the remaining neighbors among the adjacent eight candidates should be added to an expandable frozen set $\mathbf{F}_1$. Therefore, in the second iteration, the nonfrozen neighbors of $\mathbf{p}_2$ are evaluated and the connecting point $\mathbf{p}_3$ could be selected. During the front propagation segmentation, the contour member $\mathbf{p}_k$ should satisfy

$$\forall \mathbf{p}_i \in \mathbf{N}_{k-1} \ \wedge \ \mathbf{p}_i \notin \mathbf{F}_{k-1}, \quad \mathcal{M}_{\mathbf{p}_k} = \min\left\{\mathcal{M}_{\mathbf{p}_i}\right\} \tag{22}$$

where $\mathbf{N}_{k-1}$ denotes the eight neighbors of contour point $\mathbf{p}_{k-1}$ as identified in the latest iteration, and $\mathbf{F}_{k-1}$ denotes all frozen elements in the previous $(k-1)$ steps. Following the above principle, the contour can be sequentially segmented based on the arrival time map $\mathcal{M}$, as shown in Fig. 4(b).

To locate the other end of the suture thread, a specific stop criterion should be introduced in the iterative computation. By using the contour of a suture thread outlined in Fig. 5, the key points numbered as $\{\mathbf{p}_2, \mathbf{p}_3, \ldots, \mathbf{p}_j, \ldots\}$ share one high-velocity contour path when traveling to the tip $\mathbf{p}_t$, as denoted by the orange line. Apart from the first path, there also exists a second path with a high traveling speed, as indicated by the pink line. The overall contour of the suture thread can be treated as a semisymmetric object. When computing the minimal increasing manipulation iteratively, there would exist a turning point $\mathbf{p}_{\text{turn}}$ after which the following point $\mathbf{p}_k$

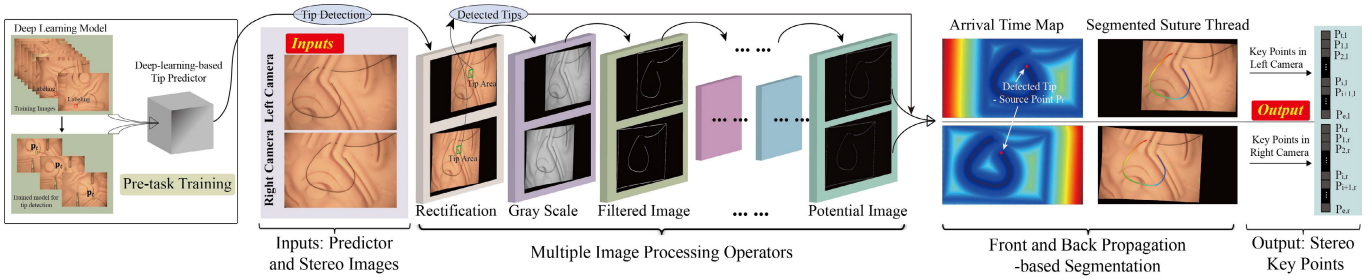

Fig. 6. Workflow of the suture thread segmentation in a calibrated stereocamera system. The inputs are the stereoimages. With the pretrained tip predictor, multiple image operators, and the arrival time-based segmentation, the key points of the suture thread in two images can be obtained. They can be utilized to obtain the final output of its 3-D coordinates.

holds the inequality $\mathcal{M}_{\mathbf{p}_k} < \mathcal{M}_{\mathbf{p}_{\text{turn}}}$. This turning phenomenon happens around the other end. Using this property, point $\mathbf{p}_{\text{turn}}$ can be treated as the end position. In the left and right cameras, these segmented points are, respectively, recorded in point sets $\mathbf{S}_l$ and $\mathbf{S}_r$. Given that the arrival time $\mathcal{M}$ of each selected pixel point cannot strictly obey the rule $\mathcal{M}_{\mathbf{p}_i} > \mathcal{M}_{\mathbf{p}_{i-1}}$ during the front propagation, a tolerance parameter χ was embedded. The final stop criteria can be defined as follows.

1) For current point $\mathbf{p}_i$, if there exist χ members in set $\{\mathbf{p}_t, \mathbf{p}_2, \mathbf{p}_3, \ldots, \mathbf{p}_{(i-1)}\}$ whose arrival times are larger than $\mathcal{M}_{\mathbf{p}_i}$, then the current point can be regarded as the turning point $\mathbf{p}_{\text{turn}}$ and the front propagation should be terminated.

At this stage, the shape of the suture thread can be initially outlined in the left and right camera frames. Given the asymmetric and irregular behavior of a suture thread, the evaluated turning point $\mathbf{p}_{\text{turn}}$ may not be the precise end of the suture thread. Therefore, a back propagation was performed to refine the segmented shape.

First, a region of interest (RoI) was created by using $\mathbf{p}_{\text{turn}}$ at the center. By combining the filtered potential image of the suture thread obtained in Section III together with the tip-refined algorithm proposed in [27], the accurate end $\mathbf{p}_e$ of the suture thread can be achieved in two camera frames.

Starting from $\mathbf{p}_e$ and evaluating the local minimal value $\mathcal{M}$ of nonfrozen neighbors, those elements belonging to the suture thread's contour can be identified via back propagation. The suture's tip $\mathbf{p}_t$ holds the property of $\mathcal{M}_{\mathbf{p}_t} = 0$. Consequently, the back propagation should be terminated when the current arrival time satisfies this condition. By recording the pixels selected in every iteration, a complete one-side contour of the suture thread with a sequence from the tip to end can be obtained in both cameras. The overall workflow of the 2-D suture thread segmentation is summarized in Fig. 6.

The 3-D suture thread can be regarded as a combination of successive subsegments. To precisely reconstruct the suture thread's shape, sufficient key point pairs that are well aligned in the rectified stereocamera must be extracted. For any key point $\mathbf{p}_{i,l}$ along the suture thread in the left camera, there should exist one point $\mathbf{p}_{j,r}$ in the right camera to the extent that these two points have the same image row number and vice versa. In other words, i and j should be equal. The total segmented points along the suture thread in both camera

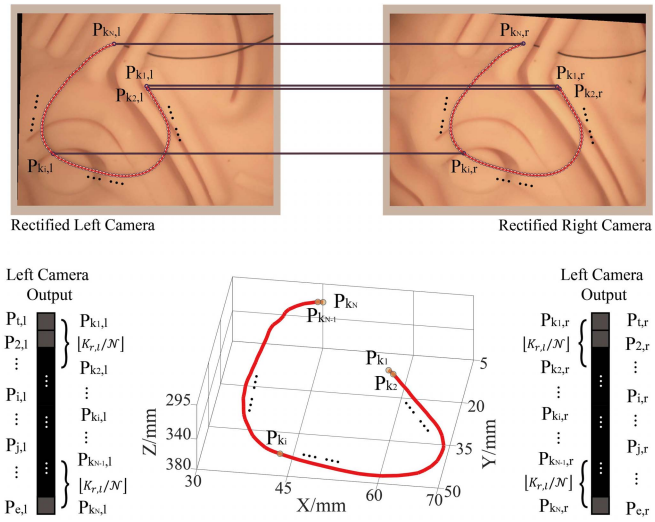

Fig. 7. Key point matching and 3-D shape computation of the suture thread based on rectified image pairs in a stereocamera.

frames must also be equal to each other, and we denote this number using the parameter $K_{r,l}$.

To select $\mathcal{N}$ key points from the segmented points' set, the tip point can be regarded as $\mathbf{p}_{k_1,l}$ and $\mathbf{p}_{k_1,r}$. As shown in Fig. 7, we selected one point from $\mathbf{S}_l = [\mathbf{p}_{t,l}, \mathbf{p}_{2,l}, \mathbf{p}_{3,l}, \ldots, \mathbf{p}_{e,l}]$ and $\mathbf{S}_r = [\mathbf{p}_{t,r}, \mathbf{p}_{2,r}, \mathbf{p}_{3,r}, \ldots, \mathbf{p}_{e,r}]$ in every $\lfloor K_{r,l}/\mathcal{N} \rfloor$ element. These contour points can be repositioned to the centerline of the suture body by using the refinement method presented in [27]. For the obtained 2-D key point pairs $\mathbf{p}_{k_i,l} = [u_{i,l}, v_{i,l}]$ and $\mathbf{p}_{k_i,r} = [u_{i,r}, v_{i,r}]$, their 3-D coordinates $\mathbf{p}_{k_i} = [X_i, Y_i, Z_i]$ can be computed as

$$\begin{cases} X_i = u_{i,l} \cdot Z_i / \mathcal{F} \\ Y_i = u_{i,l} \cdot Z_i / \mathcal{F} \\ Z_i = \mathcal{F} \cdot b / (u_{i,l} - u_{i,r}) \end{cases} \tag{23}$$

where $\mathcal{F}$ and b denote the focal and the baseline lengths of the stereocamera, respectively. Therefore, the 3-D coordinates of the suture thread with respect to the camera can be computed and illustrated point by point.

The contents presented in Section IV-C are the stereomatching approach, and its pseudocodes are listed in Algorithm 2.

Algorithm 2 Vision-Based Algorithm of Image Segmentation and Stereomatching for 3-D Shape Reconstruction of a Suture Thread in a Stereocamera System

Data: Based on stereo images and tip predictor, we obtained arrival time map $\mathcal{M}_l$ and $\mathcal{M}_r$, source points $\mathbf{p}_{t,l}$ and $\mathbf{p}_{t,r}$. Take one frame as an example and ignore the subscript l and r.

The tolerance, the current iteration number, point, arrival time, frozen set, and valid contour point are set as χ, $c = 1$, $\mathbf{p}_c = \mathbf{p}_t$, $\mathcal{M}_c = \mathcal{M}_{\mathbf{p}_t} = 0$, $\mathbf{F}_1 = Null$, and $\mathbf{S} = \mathbf{p}_t$;
while $I_N < \chi$ **do**
  Set the inspect number as $I_N = 0$;
  Increase iteration number as $c = c + 1$;
  if $\forall \boldsymbol{p}_i \in \boldsymbol{N}_{c-1} and \notin \boldsymbol{F}_{c-1}$ **then**
    Evaluate each patch $\mathcal{M}_{\mathbf{p}_i}$;
    Find the point obtains the minimal arrival → Treat it as the current contour point $\mathbf{p}_c$ → Add it to $\mathbf{S}$;
    Add $\mathbf{p}_c$ and remaining neighbors to $\mathbf{F}_c$;
    for *each* $\boldsymbol{p}_j \in \boldsymbol{S}$ **do**
      if $\mathcal{M}_{\boldsymbol{p}_j} \geqslant \mathcal{M}_{\boldsymbol{p}_c}$ **then**
        $I_N = I_N + 1$;
The last element of $\mathbf{S}$ is $\mathbf{p}_{turn}$ → Adopt the contour closure algorithm → The optimized $\mathbf{p}_e$ can be obtained;
According to **Step 1**, reset the corresponding parameters as $c = 1$, $\mathbf{p}_c = \mathbf{p}_e$, $\mathbf{F}_1 = Null$, and $\mathbf{S} = \mathbf{p}_e$;
while $\mathcal{M}_{\boldsymbol{p}_c} \neq 0$ **do**
  Repeating Step 5∼8 → Iteratively update the point set of the segmented suture thread;
Set the desired key points number as $\mathcal{N}$;
Pick out the selected points in the left and right camera → Apply key points optimizer → Locate key points to the centerline of the suture thread;
Compute the 3-D coordinates of these key points wrt. the stereo-camera;

Result: The key points' coordinates and the 3-D shape of the suture thread with respect to the camera coordinate.

V. Experimental Results and Discussion

To comprehensively evaluate the feasibility and robustness of our proposed scheme with multiple operators, we performed validations from three aspects. First, we examined the feasibility of detecting the suture thread's tip using the deep-learning model. Second, we verified the performance of the 2-D segmentation algorithm by using different backgrounds filled with noise. Third, we validated key point matching and 3-D shape computation of the suture thread by using the stereomatching algorithm.

A. Performance Validation of the Deep-Learning Model

To thoroughly validate the performance of the deep-learning-based method, three types of data based on different materials were adopted in our training and testing experiments. To label the ground truth of the suture thread's tip in each image, a bounding box with two pixels that represent the left top and right bottom locations was manually created. By setting the width of the squared bounding box to 32 pixels, all images in the database were labeled with their corresponding bounding boxes that were stored in ***json*** format.

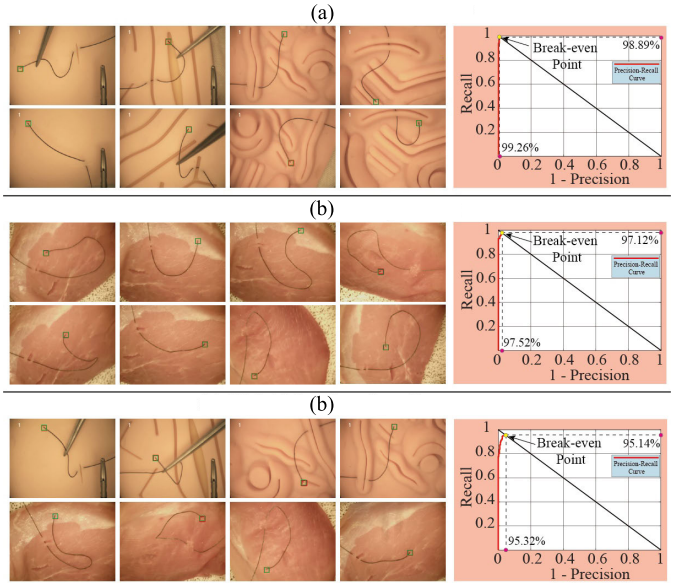

Fig. 8. Typical results and precision–recall curves of the deep-learning model for the tip detection based on the background of (a) artificial tissue, (b) porcine tissue, and (c) hybrid data.

In the first set, we acquired 1278 labeled images on various artificial tissues, of which 923 images were used for training and the remaining 355 images were adopted for testing. We prepared the second set of data by using porcine tissue and obtained 1215 labeled images, among which 972 were used for training and the remaining 243 were adopted for testing. In the last set, we combined the training data from the previous two sets to train a new model for tip prediction and then used the remaining combined images to test the new model.

We set the batch size to 1 and then applied root-mean-square propagation (RMSprop) as the optimizor with a learning rate of 0.001. We trained the model on a workstation with a Nvidia Quadro P5200 GPU. After 10 000 iterations, which were almost 11 epochs, the model converged with high accuracy. Images of the testing results from the three groups are shown in Fig. 8. The processing time for tip detection by using the trained predictor is 0.28 s per testing image.

In Fig. 8, the red squares indicate the prediction candidates, while the green squares denote the final selection of the suture thread's tip location using the Hungarian algorithm. The precision–recall curves are also shown in this figure, and detailed information regarding the precision, recall, and F1-score can be found in Table II. The high-quality performance of this deep-learning-based approach confirms that the model has a satisfactory detection performance compared with the other general methods used in object recognition tasks. Compared with common data sets, such as MNIST and CIFAR [41], which require more than 10 000 training images for building an object detection model, the deep-learning

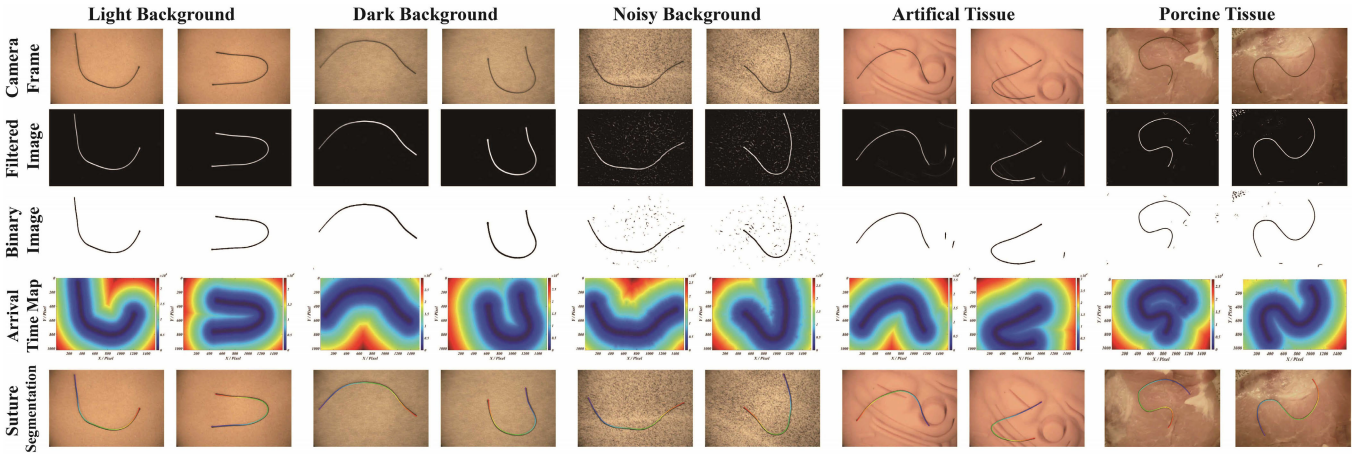

Fig. 9. Experimental results of a suture thread detection with different backgrounds. Pure light and dark backgrounds were implemented in the first and second groups. In the third trial, noises were randomly added, and the artificial tissue and porcine were adopted in the fourth and fifth groups.

TABLE II
PERFORMANCE VALIDATION OF THE DEEP-LEARNING MODEL BASED ON DIFFERENT BACKGROUNDS

Background	Precision	Recall	F1-score
Artificial Tissue	99.63%	98.89%	99.26%
Porcine Tissue	97.93%	97.12%	97.52%
Hybrid Backgrounds	95.51%	95.14%	95.32%

method adopted in this article can train a model for accurate tip detection by using less than 1000 training images.

B. Validation of Suture Thread's Segmentation

To test the robustness of the segmentation algorithm, we examined a suture thread in five different scenarios. We also performed three trials in each scenario, with two trials shown in Fig. 9. In the first scenario, a pure background that shows an obvious color contrast to the suture thread was adopted. By using the arrival time map and the detected tip point that was treated as the source point, the suture thread can be successfully segmented from the background, whereas its key points can be obtained in the image.

To further test the robustness, the color contrast between the suture and the background was decreased, and the environmental disturbance was increased by randomly adding noises to the background in the second and third scenarios. According to the results, the suture thread's shape was successfully segmented by the proposed scheme. In the last two groups, the experiment was performed on an artificial tissue and porcine meat. The results successfully validate the efficacy of our algorithm for the 2-D shape segmentation of suture thread.

1) Precision of Exit Point Detection: Detecting the suture's exit point plays an important role in determining the completeness of its 2-D segmentation, the precision of the stereo key point matching, and the overall 3-D length computation. To validate its accuracy, we compared the detected exit points in the front and back propagations with the manually labeled ones. The detailed results are recorded in Table III.

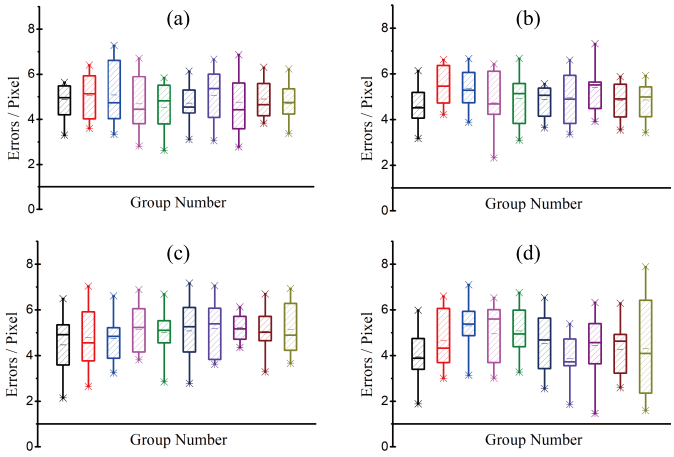

Fig. 10. Box plot of 2-D segmentation errors based on random key points' validations from a total of 40 experiments. (a) Artificial tissue 1. (b) Artificial tissue 2. (c) Porcine with strong light. (d) Porcine with dark light.

The turning point was initially figured out by using the proposed stop criterion during the front propagation. The turning point shows larger errors (between 10 and 20 pixels) than the ground truth. The back propagation can then efficiently decrease these errors to around 5 pixels and significantly enhance the output of the 2-D suture thread segmentation task.

2) Accuracy of Suture Thread Segmentation: After detecting the two ends and the arrival time map, the complete suture thread can be segmented. To validate the accuracy of the curvilinear shape segmentation, two artificial tissues and two porcine tissues under different light intensities were examined. The suture thread on the tissues was stitched arbitrarily to form various shapes. Afterward, ten random key points along the suture were manually selected as ground truth, and their position errors with respect to the segmented suture in 2-D were evaluated. For each background, ten experiments were conducted. The mean errors concerning the units of pixels and millimeters are listed in Table IV, and the error variation in each experiment was computed by using a box plot, as shown in Fig. 10. It is noticed that the largest error

TABLE III

EXPERIMENTS OF A SUTURE THREAD'S EXIT POINT DETECTION AMONG DIFFERENT BACKGROUNDS

Backgrounds	$\{\mathcal{R}_{b,\sigma_i}, \mathcal{S}_{\sigma_i}\}$	Exit Position Computation of a Pierced Suture Thread Using the Front and Back Propagation; Unit: Pixel								
		Experiment 1			**Experiment 2**			**Experiment 3**		
		Labeling	Computed Results		Labeling	Computed Results		Labeling	Computed Results	
			Initial	Rectified		Initial	Rectified		Initial	Rectified
Light Color	{1,15}	(1215,514)	(1213,531)	(1216,512)	(1252,924)	(1235,932)	(1251,923)	(525,322)	(520,320)	(521,320)
Dark Color	{2.4,10}	(525,361)	(521,374)	(526,357)	(1381,615)	(1381,602)	(1382,617)	(630,402)	(615,409)	(627,397)
With Noises	{1.5,16}	(1425,442)	(1415,454)	(1421,442)	(372,169)	(362,166)	(375,173)	(512,503)	(512,516)	(516,501)
Artificial Tissue	{2.5,14}	(193,679)	(196,699)	(191,681)	(876,913)	(868,922)	(876,914)	(595,316)	(589,310)	(598,315)
Porcine	{2,6}	(843,766)	(840,763)	(840,767)	(1020,126)	(1023,122)	(1023,124)	(1060,733)	(1043,733)	(1062,729)

TABLE IV

MEAN ERRORS OF A SUTURE THREAD'S SEGMENTATION BASED ON RANDOM POINTS' VALIDATIONS. UNIT: PIXEL AND mm

Group Number	Artificial Tissue 1	Artificial Tissue 2	Porcine with Strong Light	Porcine with Dark Light
#1	4.35&0.22	4.35&0.22	4.81&0.24	4.74&0.24
#2	5.14&0.26	5.14&0.26	4.81&0.24	4.29&0.21
#3	5.27&0.26	5.27&0.26	5.10&0.26	4.49&0.22
#4	4.96&0.25	4.96&0.25	4.33&0.22	4.66&0.23
#5	4.84&0.24	4.84&0.24	5.00&0.25	4.24&0.21
#6	4.72&0.24	4.72&0.24	5.23&0.26	4.11&0.21
#7	4.94&0.25	4.94&0.25	5.83&0.29	3.78&0.19
#8	3.89&0.19	3.89&0.19	4.34&0.22	4.74&0.24
#9	5.03&0.25	5.03&0.25	5.66&0.28	5.03&0.25
#10	5.04&0.25	5.04&0.25	4.66&0.23	5.19&0.26

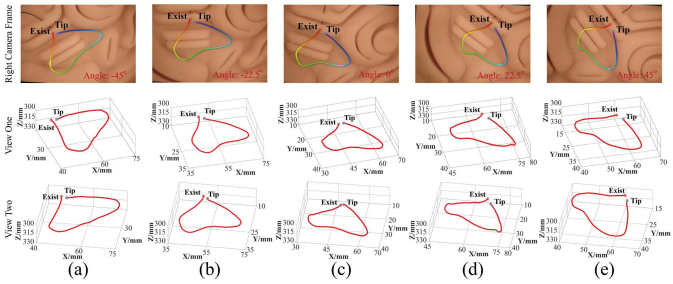

Fig. 11. Computed 3-D shape of a suture thread with a rotation angle of (a) −45°, (b) −22.5°, (c) 0°, (d) 22.5°, and (e) 45°. The suture thread was formed in a semiheart shape.

was around 8 pixels/0.4 mm, and the average error values were all below 6 pixels/0.3 mm. These tests prove that our method can enable an accurate suture thread segmentation with key points generated along the suture for the following 3-D reconstruction.

C. 3-D Coordinates Computation of the Suture Thread

1) Evaluating the Consistency of Suture Thread 3-D Computation: To examine the 3-D computational accuracy of the suture's length, we initially measured the actual length between the tip and exit point. In the first test, we performed suture thread tracking by using the suture to form a semi-heart shape. As shown in Fig. 11, the orientation of the tissue was then changed from −45° to 45° at an increment of 22.5°. By rotating the tissue to different orientations, its corresponding shape and length in 3-D can be obtained, and the robustness of the vision-based algorithm can be evaluated.

TABLE V

COMPUTED 3-D LENGTHS AND ERRORS OF A SUTURE THREAD WITH DIFFERENT ORIENTATION ANGLES ON THE WORKING PLANE (GROUND TRUTH LENGTH: 85 mm)

Orientation	-45°	-22.5°	0°	22.5°	45°
Length(mm)	85.97	86.36	85.87	83.89	84.85
Error(mm)	0.97	1.36	0.87	1.11	0.15
Error ratio	1.14%	1.60%	1.02%	1.31%	0.18%

In the figure, the segmented sutures were highlighted in colored curves and the 3-D shapes were shown from two view angles. The computed lengths are presented in Table V. It can be seen that the detection errors were all below 1.5 mm and the error-to-length percentages were within 2%. Considering the workspace used for the experiments, this amount of error is fairly accurate to achieve a reliable automated tool manipulation for grasping the suture thread.

2) Quantitative Evaluation of Suture Thread's 3-D Length Computation: To further validate the performance of the proposed method, we utilized three artificial tissues and two porcine meats as backgrounds. The suture thread was then fixed to different lengths in each experimental set, and six experiments with variant backgrounds and suture's orientations/locations were carried out. Two experimental results from each set are shown in Fig. 12, and the remaining outcomes are presented in the Supplementary Material.

In the first set, the length was fixed at 50 mm. Fig. 12(a) presents the segmented shape, the arrival time map, and the 3-D coordinates of the suture thread with respect to the camera coordinate. To clearly observe its 3-D shape, the results are also shown from two view angles. Based on the acquisition of the stereo key point pairs of the suture thread, its spatial coordinates can be obtained by using the triangulation relationship. By comparing its 3-D structure to the ground truth, the overall shape appears to be correctly constructed.

In the second and third sets, the suture's lengths increased to 80 and 100 mm, respectively. As shown in Fig. 12(b) and (c), the suture can be successfully detected and its 3-D shape is highlighted by using the red curve. The porcine tissues were used in the fourth and fifth sets to validate the practical feasibility of our approach. With different light intensities, it can be noticed that the 3-D information of the suture thread can be achieved regardless of its location and orientation.

Moreover, the computed lengths are presented in Table VI. Compared with the ground truth, the maximum error in the

TABLE VI

COMPUTATIONAL RESULTS FOR THE OVERALL 3-D LENGTH OF SUTURE THREADS IN DIFFERENT SCENARIOS. UNIT: mm

Experiment Set	Ground Truth	Experiment 1		Experiment 2		Experiment 3		Experiment 4		Experiment 5		Experiment 6		Error Analysis	
		Result	Error	Result	Error	Result	Error	Result	Error	Result	Error	Result	Error	Average	Maximal
Set 1	50	49.95	0.05	49.93	0.07	49.79	0.21	50.64	0.64	49.83	0.17	50.90	0.90	0.34	0.90
Set 2	80	79.90	0.10	79.12	0.88	79.89	0.11	79.99	0.01	80.22	0.22	80.47	0.47	0.30	0.88
Set 3	100	100.67	0.67	101.74	1.74	99.89	0.11	101.01	1.01	100.68	0.68	99.24	0.76	0.83	1.74
Set 4	100	99.02	0.98	99.46	0.54	100.29	0.29	98.86	1.14	100.95	0.95	99.92	0.08	0.66	1.14
Set 5	100	99.03	0.97	98.49	1.51	99.39	0.61	98.80	1.20	98.46	1.54	99.71	0.29	1.02	1.54

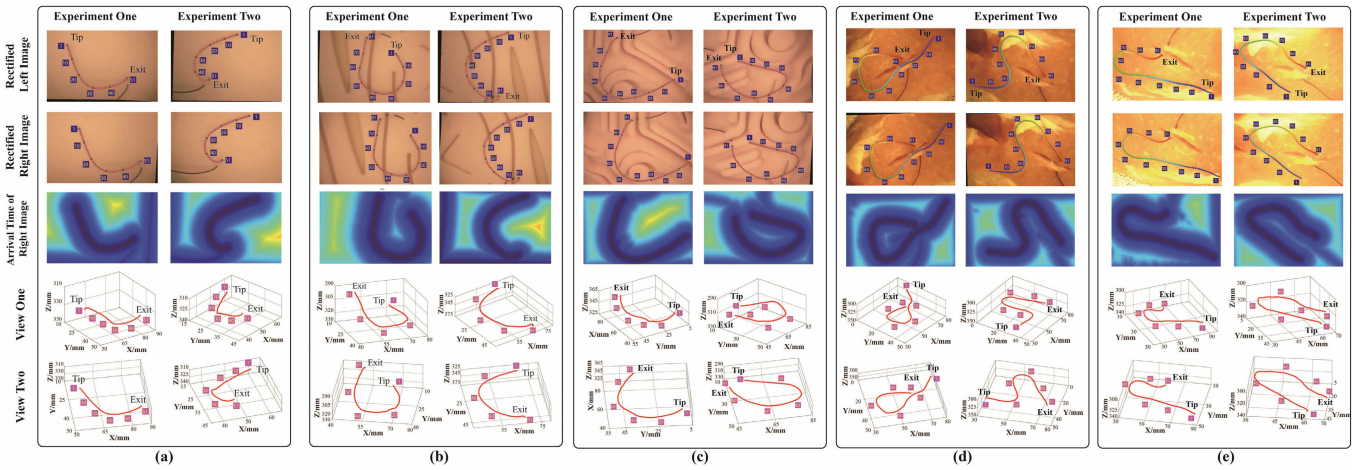

Fig. 12. Typical results of the overall 3-D shape computation of the suture thread. Key points' correspondences were figured out along the suture thread in the stereocamera system. The suture length and the background were set as (a) 50 mm—artificial tissue 1, (b) 80 mm—artificial tissue 2, (c) 100 mm—artificial tissue 3, (d) 100 mm—porcine tissue with dark light, and (e) 100 mm—porcine tissue with strong light.

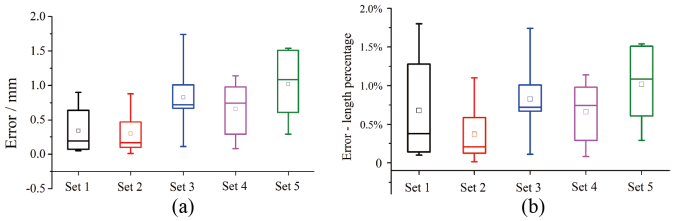

Fig. 13. Box plot of errors for the computed 3-D length of a suture thread in various conditions. (a) Absolute errors. (b) Corresponding error-to-length ratios in each experimental set.

first group was 0.90 mm. Increasing the total length also increases the computed errors. With a ground truth of 100 mm in set 3, the largest error reached 1.74 mm in experiment 2. Compared with the total length, the error-to-length ratio was only 1.74% in this condition. In all 30 experiments, the maximum value of this ratio was only 1.8%, which happened in set 1 experiment 6.

Referring to the workflow in Figs. 6 and 7, the majority of the computational time was spent on generating the arrival time map. Given the different resolutions of the input camera frames, the time consumption varies from 30 to 120 s for each camera. All the other steps in the 3-D suture thread reconstruction can be finished within 10–20 s.

Compared with [42], which focused on catheter tip detection, this article aims to provide a comprehensive solution toward figuring out not only the suture's tip but also its entire shape. Besides, our tip detection error can be limited to within 0.5 mm, which is more accurate compared with the minimal error of 3.7 mm reported in [42]. For the work in [43], they mainly studied the segmentation of the suture thread in a 2-D condition. In this article, we extensively considered suture's 3-D reconstruction by using a stereocamera, and the physical length of the suture thread in various conditions was evaluated. In [16], the procedure requires a manual selection of one suture's endpoint, and the accuracy in evaluating the length depends on the selected mathematical model to represent the current suture's shape. However, in this article, the computation can be initialized by using a deep-learning model, and we proposed a model-free approach. Besides, the maximal error-to-length ratio is only 1.8% as shown in Fig. 13, which is more accurate than the value of 4.75% reported in [16].

VI. CONCLUSION

In this article, we presented a novel stereovision-based algorithm to reconstruct the 3-D coordinates of a suture thread. To automate the procedure, a deep-learning model was implemented to detect the suture thread's tip. An image filter with multiple image preprocessing operators was built to enhance the curvilinear structure of the suture thread while eliminating environmental noise. To precisely and completely describe the suture thread, a novel concept based on the arrival time of the propagation, which was calculated based on the multistencils fast marching principle, was adopted. Based on this knowledge, the suture thread can be segmented by using the front propagation algorithm and efficiently refined through the back propagation approach. Contours of the

suture with zigzag or redundant paths can be eliminated, thereby ensuring the precision of key points' matching and 3-D shape computation in the stereocamera. The accuracy of the deep-learning model for suture's tip detection was examined by using different backgrounds. The performance of the proposed approach in 2-D image segmentation, 3-D shape reconstruction, and spatial length computation of the suture thread was then comprehensively and successfully validated across various experimental scenarios.

Based on these findings, our approach can be successfully implemented to compute the 3-D length and coordinates of a surgical suture thread, thereby reducing the human intervention and facilitating an automated manipulation of the vision-based suture thread grasping task by using a robot, which gives a promising future of achieving a higher level of automation in the task of robot-assisted surgical knot tying.

REFERENCES

[1] G. I. Barbash and S. A. Glied, "New technology and health care costs—The case of robot-assisted surgery," *New England J. Med.*, vol. 363, pp. 701–704, 2010.

[2] K. Moorthy *et al.*, "Dexterity enhancement with robotic surgery," *Surg. Endosc. Intervention. Techn.*, vol. 18, no. 5, pp. 790–795, 2004.

[3] R. Konietschke, T. Ortmaier, H. Weiss, G. Hirzinger, and R. Engelke, "Manipulability and accuracy measures for a medical robot in minimally invasive surgery," in *On Advances in Robot Kinematics*. Dordrecht, The Netherlands: Springer, 2004, pp. 191–198.

[4] J. Marescaux *et al.*, "Transatlantic robot-assisted telesurgery," *Nature*, vol. 413, pp. 379–380, Sep. 2001.

[5] C. Freschi, V. Ferrari, F. Melfi, M. Ferrari, F. Mosca, and A. Cuschieri, "Technical review of the da Vinci surgical telemanipulator," *Int. J. Med. Robot. Comput. Assist. Surgery*, vol. 9, no. 4, pp. 396–406, 2013.

[6] R. Berguer, "Surgery and ergonomics," *Arch. Surgery*, vol. 134, no. 9, pp. 1011–1016, 1999.

[7] G. P. Moustris, S. C. Hiridis, K. M. Deliparaschos, and K. M. Konstantinidis, "Evolution of autonomous and semi-autonomous robotic surgical systems: A review of the literature," *Int. J. Med. Robot. Comput. Assist. Surgery*, vol. 7, no. 4, pp. 375–392, 2011.

[8] B. Lu, H. K. Chu, and L. Cheng, "Robotic knot tying through a spatial trajectory with a visual servoing system," in *Proc. IEEE/RSJ Int. Conf. Intell. Robots Syst. (IROS)*, Sep. 2017, pp. 5710–5716.

[9] B. Lu, H. K. Chu, K. C. Huang, and L. Cheng, "Vision-based surgical suture looping through trajectory planning for wound suturing," *IEEE Trans. Autom. Sci. Eng.*, vol. 16, no. 2, pp. 542–556, Apr. 2019.

[10] C. R. Wagner, N. Stylopoulos, P. G. Jackson, and R. D. Howe, "The benefit of force feedback in surgery: Examination of blunt dissection," *Presence*, vol. 16, no. 3, pp. 252–262, Jun. 2007.

[11] S. Sen, A. Garg, D. V. Gealy, S. McKinley, Y. Jen, and K. Goldberg, "Automating multi-throw multilateral surgical suturing with a mechanical needle guide and sequential convex optimization," in *Proc. IEEE Int. Conf. Robot. Automat. (ICRA)*, May 2016, pp. 4178–4185.

[12] S. A. Pedram, P. Ferguson, J. Ma, E. Dutson, and J. Rosen, "Autonomous suturing via surgical robot: An algorithm for optimal selection of needle diameter, shape, and path," in *Proc. IEEE Int. Conf. Robot. Automat. (ICRA)*, May 2017, pp. 2391–2398.

[13] T. Osa, N. Sugita, and M. Mitsuishi, "Online trajectory planning and force control for automation of surgical tasks," *IEEE Trans. Autom. Sci. Eng.*, vol. 15, no. 2, pp. 675–691, Apr. 2018.

[14] G. Mohanarajah, V. Usenko, M. Singh, R. D'Andrea, and M. Waibel, "Cloud-based collaborative 3D mapping in real-time with low-cost robots," *IEEE Trans. Autom. Sci. Eng.*, vol. 12, no. 2, pp. 423–431, Apr. 2015.

[15] H. Ren, W. Liu, and A. Lim, "Marker-based surgical instrument tracking using dual Kinect sensors," *IEEE Trans. Autom. Sci. Eng.*, vol. 11, no. 3, pp. 921–924, Jul. 2014.

[16] R. C. Jackson, R. Yuan, D.-L. Chow, W. S. Newman, and M. C. Çavuşoğlu, "Real-time visual tracking of dynamic surgical suture threads," *IEEE Trans. Autom. Sci. Eng.*, vol. 15, no. 3, pp. 1078–1090, Jul. 2018.

[17] B. Obara, M. Fricker, D. Gavaghan, and V. Grau, "Contrast-independent curvilinear structure detection in biomedical images," *IEEE Trans. Image Process.*, vol. 21, no. 5, pp. 2572–2581, May 2012.

[18] F. Benmansour and L. D. Cohen, "Fast object segmentation by growing minimal paths from a single point on 2D or 3D images," *J. Math. Imag. Vis.*, vol. 33, no. 2, pp. 209–221, Feb. 2009.

[19] V. Kaul, A. Yezzi, and Y. Tsai, "Detecting curves with unknown endpoints and arbitrary topology using minimal paths," *IEEE Trans. Parallel Distrib. Syst.*, vol. 34, no. 10, pp. 1952–1965, Oct. 2012.

[20] Y.-J. Cha, W. Choi, and O. Büyüköztürk, "Deep learning-based crack damage detection using convolutional neural networks," *Comput.-Aided Civil Infrastruct. Eng.*, vol. 32, no. 5, pp. 361–378, 2017.

[21] Y.-J. Cha, W. Choi, G. Suh, S. Mahmoudkhani, and O. Büyüköztürk, "Autonomous structural visual inspection using region-based deep learning for detecting multiple damage types," *Comput.-Aided Civil Infrastruct. Eng.*, vol. 33, no. 9, pp. 731–747, Sep. 2018.

[22] F.-C. Chen and M. R. Jahanshahi, "NB-CNN: Deep learning-based crack detection using convolutional neural network and Naïve Bayes data fusion," *IEEE Trans. Ind. Electron.*, vol. 65, no. 5, pp. 4392–4400, May 2018.

[23] R. Stewart, M. Andriluka, and A. Y. Ng, "End-to-end people detection in crowded scenes," in *Proc. IEEE Conf. Comput. Vis. Pattern Recognit.*, Jun. 2016, pp. 2325–2333.

[24] X. Qian *et al.*, "A non-parametric vessel detection method for complex vascular structures," *Med. Image Anal.*, vol. 13, no. 1, pp. 49–61, 2009.

[25] M. S. Hassouna and A. A. Farag, "Multistencils fast marching methods: A highly accurate solution to the Eikonal equation on Cartesian domains," *IEEE Trans. Pattern Anal. Mach. Intell.*, vol. 29, no. 9, pp. 1563–1574, Sep. 2007.

[26] D. Chen, J.-M. Mirebeau, and L. D. Cohen, "Vessel tree extraction using radius-lifted keypoints searching scheme and anisotropic fast marching method," *J. Algorithms Comput. Technol.*, vol. 10, no. 4, pp. 224–234, 2016.

[27] B. Lu, H. K. Chu, K. C. Huang, and J. W. Lai, "Surgical suture thread detection and 3D reconstruction using a model-free approach in a calibrated stereo-visual system," *IEEE/ASME Trans. Mechatronics*, to be published, doi: 10.1109/TMECH.2019.2942715.

[28] C. Goutte, F. A. Nielsen, and K. H. Hansen, "Modeling the hemodynamic response in fMRI using smooth FIR filters," *IEEE Trans. Med. Imag.*, vol. 19, no. 12, pp. 1188–1201, Dec. 2000.

[29] G. Deng and L. W. Cahill, "An adaptive Gaussian filter for noise reduction and edge detection," in *Proc. IEEE Conf. Rec. Nucl. Sci. Symp. Med. Imag. Conf.*, Oct. 1993, pp. 1615–1619.

[30] P. W. Verbeek, H. A. Vrooman, and L. J. Van Vliet, "Low-level image processing by max-min filters," *Signal Process.*, vol. 15, no. 3, pp. 249–258, 1998.

[31] S.-J. Ko and Y. H. Lee, "Center weighted median filters and their applications to image enhancement," *IEEE Trans. Circuits Syst.*, vol. 38, no. 9, pp. 984–993, Sep. 1991.

[32] C. Steger, "An unbiased detector of curvilinear structures," *IEEE Trans. Pattern Anal. Mach. Intell.*, vol. 20, no. 2, pp. 113–125, Feb. 1998.

[33] A. F. Frangi, W. J. Niessen, K. L. Vincken, and M. A. Viergever, "Multiscale vessel enhancement filtering," in *Proc. Int. Conf. Med. Image Comput. Comput.-Assist. Intervent.*, vol. 1496. Berlin, Germany: Springer, 1998, pp. 130–137.

[34] T. Lindeberg, "Edge detection and ridge detection with automatic scale selection," *Int. J. Comput. Vis.*, vol. 30, no. 2, pp. 117–156, 1998.

[35] C. Lorenz, I.-C. Carlsen, T. M. Buzug, C. Fassnacht, and J. Weese, "Multi-scale line segmentation with automatic estimation of width, contrast and tangential direction in 2D and 3D medical images," in *CVRMed-MRCAS* (Lecture Notes in Computer Science). Berlin, Germany: Springer, 1997, pp. 233–242.

[36] J. Jin, L. Yang, X. Zhang, and M. Ding, "Vascular tree segmentation in medical images using Hessian-based multiscale filtering and level set method," *Comput. Math. Methods Med.*, vol. 2013, Oct. 2013, Art. no. 502013.

[37] D. Adalsteinsson and J. A. Sethian, "A fast level set method for propagating interfaces," *J. Comput. Phys.*, vol. 118, no. 2, pp. 269–277, 1995.

[38] E. Rouy and A. Tourin, "A viscosity solutions approach to shape-from-shading," *SIAM J. Numer. Anal.*, vol. 29, no. 3, pp. 867–884, 2006.

[39] J. A. Sethian, *Level Sets Methods and Fast Marching Methods*. Cambridge, U.K.: Cambridge Univ. Press, 1999.

[40] A. Fusiello, E. Trucco, and A. Verri, "A compact algorithm for rectification of stereo pairs," *Mach. Vis. Appl.*, vol. 12, no. 1, pp. 16–22, 2000.

[41] W. Rawat and Z. Wang, "Deep convolutional neural networks for image classification: A comprehensive review," *Neural Comput.*, vol. 29, no. 9, pp. 2352–2449, 2017.
[42] H. Lee, M. Mansouri, S. Tajmir, M. H. Lev, and S. Do, "A deep-learning system for fully-automated peripherally inserted central catheter (PICC) tip detection," *J. Digit. Imag.*, vol. 31, no. 4, pp. 393–402, 2018.
[43] Y. Hu, Y. Gu, J. Yang, and G.-Z. Yang, "Multi-stage suture detection for robot assisted anastomosis based on deep learning," in *Proc. IEEE Int. Conf. Robot. Automat. (ICRA)*, May 2018, pp. 1–8.

Bo Lu received the B.Eng. degree from the Department of Ship and Offshore Engineering, Dalian University of Technology, Dalian, Liaoning, China, in 2013, and the M.S. (Hons.) and Ph.D. degrees from the Department of Mechanical Engineering, The Hong Kong Polytechnic University, Hong Kong, in 2015 and 2019, respectively.

He is currently a Post-Doctoral Research Fellow with the T Stone Robotics Institute, The Chinese University of Hong Kong, Hong Kong. His current research interests include medical robotics, computer vision, vision-based manipulation, automation and control, trajectory plan, surgical tool detection, surgical procedure analysis, and understanding.

X. B. Yu received the B.Eng. degree from Zhejiang Chinese Medical University, Zhejiang, China, in 2012, and the M.S. degree from The Hong Kong Polytechnic University, Hong Kong, in 2015, where he is currently pursuing the Ph.D. degree with the Department of Computing.

His research interests include big data analytics, machine learning, data mining, artificial intelligence, deep learning, and software engineering.

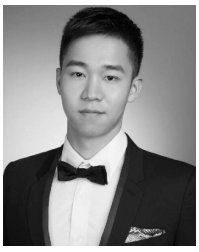

J. W. Lai received the B.Eng. degree from the Department of Metallurgical Engineering, Wuhan University of Science and Technology, Wuhan, China, in 2016, and the M.Sc. degree from the Department of Mechanical and Automation Engineering, The Chinese University of Hong Kong, Hong Kong, in 2017. He is currently pursuing the Ph.D. degree with The Hong Kong Polytechnic University, Hong Kong.

His research interests include continuum robot, soft robot, robotic control, computer vision, and surgical robot systems.

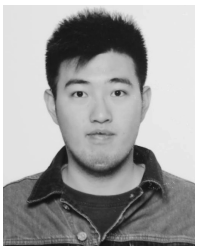

K. C. Huang received the B.Eng. degree in automation from the Department of Mechatronic and Control Engineering, Shenzhen University, Shenzhen, Guangdong, China, in 2014, and the M.Sc. degree in mechanical and automation engineering from The Chinese University of Hong Kong, Hong Kong, in 2015. He is currently pursuing the Ph.D. degree with the Department of Mechanical Engineering, The Hong Kong Polytechnic University, Hong Kong.

His research interests include automated cell patterning with dielectrophoresis.

Keith C. C. Chan received the B.Math. degree (Hons.) in computer science and statistics and the M.A.Sc. and Ph.D. degrees in systems design engineering from the University of Waterloo, Waterloo, ON, Canada, in 1984, 1985, and 1989, respectively.

He then worked as a Software Analyst for the development of multimedia and software engineering tools with the IBM Canada Laboratory, Toronto, ON, Canada. In 1994, he joined The Hong Kong Polytechnic University, Hong Kong, where he is currently a Professor with the Department of Computing. He has authored or coauthored more than 250 publications. His research has been supported both by government research funding agencies and the industry. His research interests include big data analytics, computational biology, data mining, machine learning, evolutionary computation, and artificial intelligence.

Henry K. Chu (M'12) received the B.S. degree in mechanical engineering from the University of Waterloo, Waterloo, ON, Canada, and the M.S. and Ph.D. degrees in mechanical and industrial engineering from the University of Toronto, Toronto, ON, Canada.

He was a Post-Doctoral Fellow with the University of Toronto and the City University of Hong Kong, Hong Kong. He is currently an Assistant Professor with The Hong Kong Polytechnic University, Hong Kong. His research interests include robotic manipulation, vision-based control and automation, microsystem design, and tissue engineering.